

Supporting Information for “Model Driven Optimization of Magnetic Anisotropy of Exchange-coupled Core-Shell Ferrite Nanoparticles for Maximal Hysteretic Loss”

1-Nanoparticle Synthesis, Polymer Coating and Characterization

- 1.1 Synthesis of Co@Mn, Mn@Co, and Mn@Co-TL MNPs
- 1.2 One-pot synthesis of Co ferrite and Mn ferrite MNPs
- 1.3 Coating of MNPs using amphiphilic polymer (PMA)
- 1.4 Purification of MNPs with agarose gel electrophoresis
- 1.5 Size distribution measurements using TEM
- 1.6 Structural characterization using TEM methods
- 1.7 Dynamic light scattering (DLS) and zeta potential
- 1.8 ICP-MS analysis

2. Magnetization measurements

- 2.1 Instruments
- 2.2 Non-Interacting Super-Paramagnetic model: fit of M vs H measurements
- 2.3 Determination of Anisotropy Constant
- 2.4 M vs H data at 5K
- 2.5 M vs H Fit and χ_0 calculation
- 2.6 ZFC/FC measurements at different magnetic fields (1 mT and 10 mT)

3. Specific Loss Power (SLP)

- 3.1. Experimental equipment and measurement of SLP
- 3.2. Theoretical model: Basis of the simulation of SLP by Linear Response Theory (LRT) and quasi-Linear Response Theory (q-LRT)

1. Nanoparticles Synthesis and Characterization

Seeds, core-shell and single-phase magnetic nanoparticles (MNPs) were produced by thermal decomposition of metal precursors following largely protocols for single-phase MNPs^{1,2} or core-shell ferrite MNPs³. Materials used are listed in the method section of the manuscript.

In order to produce colloids with the desired sizes and structure (single-phase or core-shell), we combined and adapted existing methods, except for the production of Mn ferrite MNPs with $d \sim 14$ nm, which followed ². Compared to the previous core-shell ferrite synthesis³, our synthesis is greatly simplified by avoiding trioctylamine, which may have led to slightly higher dispersity.

1.1. Synthesis of of core-shell MNPs

Co@Mn MNPs. Monodisperse Co ferrite seeds ($d_{in} \sim 7$ nm) were synthesized combining previously addressed concepts and details ¹². Under an inert atmosphere, iron(III) acetylacetonate ($Fe(acac)_3$, 2 mmol, Strem, #262300), cobalt(II) acetylacetonate ($Co(acac)_2$, 1 mmol, Sigma Aldrich, #227129) and 1,2-hexadecanediol (10 mmol, Sigma Aldrich, #213748) were mixed in a 100 ml flask in the presence of 6 mmol of oleic acid (OLA, Sigma Aldrich, #O1008), 6 mmol of oleylamine (OLAM, Sigma Aldrich, #O7805), and 20 ml of benzyl ether (Sigma Aldrich, #108014). The mixture was degassed for 30 min under vacuum at 100 °C. Under nitrogen flow, the temperature was increased up to 200 °C at a heating rate of 3.3 K/min, left for 2 h at 200 °C, and then the temperature was again increased at 3.3 K/min and the reaction was heated to reflux (~ 300 °C) for 1 h. Removing the heating mantle stopped the reaction, and the black-colored mixture was cooled to room temperature (RT). Upon the addition of 40 ml of ethanol (96 %, Carl Roth, #64-17-5), a black material was precipitated by centrifugation (2888 rcf, 10 min), *i.e.*, the hydrocarbon chain-coated Co ferrite NPs. The supernatant was removed, and the black precipitate was dissolved in 20 ml toluene (Carl Roth, #9558.2) with 0.05 ml of OLA and 0.05 ml of OLAM. The solution was centrifuged (2888 rcf, 10 min) to remove aggregates (*i.e.* the precipitate was discarded). The sample was washed by adding 40 ml of ethanol, centrifuged (2888 rcf, 10 min) to remove the solvent. Lastly, the precipitate was redispersed in 20 ml of chloroform ($CHCl_3$, Carl Roth, #Y015.2), and characterized by transmission electron microscopy (TEM, Jeol 1400 plus) (Figure S1).

Monodisperse Co@Mn MNPs were synthesized by growing a shell of Mn ferrite onto the previously described Co ferrite seeds. As for the preparation of the seeds, the synthetic protocol used for the preparation of the Co@Mn MNPs was adapted from previous work regarding the seed-growth synthetic

methods for the preparation of single-phase MFe_2O_3 ($M = Fe, Mn, Co$) MNPs^{4,12}. In detail, $Fe(acac)_3$ (2 mmol), $Mn(acac)_2$ (1 mmol), 1,2-hexadecanediol (10 mmol) and 40 mg of Co ferrite seeds (dispersed in 4 ml of $CHCl_3$) were mixed in a 100 ml flask in the presence of 2 mmol of OLA, 2 mmol OLAM and 20 ml of benzyl ether. Under vacuum, the reaction mixture was firstly heated to 100 °C and kept at this temperature for 30 min to remove the $CHCl_3$. Under nitrogen, with a heating rate of 3.3 K/min, the temperature was increased to 200 °C, kept at this temperature for 1 h, and then heated to reflux (~300 °C) for 30 min. Removing the heating mantle stopped the reaction and the black-colored mixture was cooled down to RT. The cleaning step was equivalent to the process described previously. Figure S1-b shows TEM of the resultant NPs (*ca.* 13.1 nm in diameter).

Mn@Co MNPs. Mn ferrite seeds (6.9 nm) were synthesized as Co ferrite seeds above, but replacing the 1 mmol of $Co(acac)_2$ by 1 mmol of $Mn(acac)_2$ (Figure S1-c). To grow the Mn@Co MNPs, 40 mg Mn ferrite seeds dispersed in 4 ml of $CHCl_3$ were mixed with 2 mmol of $Fe(acac)_3$, 1 mmol of $Co(acac)_2$, 10 mmol of 1,2-hexadecanediol, 2 mmol of OLA, 2 mmol of OLAM, and 20 ml of benzyl ether. The further reaction protocol was the same as for Co@Mn (Figure S1-d).

Mn@Co-TL /Thin Layer MNPs. In this case, the size of the Mn ferrite core was increased from 7 to 10 nm, and the thickness of the Co ferrite shell was decreased to reach the same MNP size (*ca.* 14 nm) as the previous core shell systems. 10 nm Mn ferrite seeds were synthesized by adding $Fe(acac)_3$ (2 mmol), $Mn(acac)_2$ (1 mmol), 1,2-hexadecanediol (10 mmol), OLA (6 mmol), OLAM (6 mmol) and 10 ml benzyl ether. The further reaction protocol was the same as above (resulting MNP Figure S1-e).

The shell growth was initiated by the addition of 40 mg of 10 nm Mn ferrite seeds (dispersed in 4 ml $CHCl_3$) to the mixture of $Fe(acac)_3$ (2 mmol), $Co(acac)_2$ (1 mmol), 1,2-hexadecanediol (10 mmol), OLA (2 mmol), OLAM (2 mmol), and 20 ml of benzyl ether. The further reaction protocol was the same as for Co@Mn (Figure S1-f).

1.2. One-pot synthesis of 14nm Co ferrite MNPs and 14nm Mn ferrite MNPs

The one-pot synthesis of Co ferrite MNPs was accomplished using the following procedure: 2 mmol of Fe(acac)₃, 1 mmol of Co(acac)₂, 6 mmol of oleic acid, and 6 mmol of oleylamine were added into a 100 ml three-necked flask, as well as 10 mmol of 1,2-hexadecanediol and 17 ml of benzyl ether. After degassing at 100 °C for 30 min, the mixture was slowly heated up to 200 °C for 2 h under a N₂ flow. Then, the temperature was increased to 300 °C for 1 h. Removing the heating mantel stopped the reaction, and the black solution was precipitated with ethanol and dissolved in chloroform (Figure S1-g).

Mn ferrite MNPs were synthesized as previously described². Specifically, 2 mmol Fe(acac)₃, 1 mmol MnCl₂ were mixed with 6.31 mmol OLA, 12.16 mmol of OLAM and 2 ml of dioctyl ether. The mixture was firstly heated to 100 °C for 30 min under vacuum, using a flow of N₂ as protection, then heated to 200 °C at a heating rate of 3.3 K/min and kept at this temperature for 2 h. With the same heating speed, the temperature of the solution was increased to reflux (330°C) and kept there for 1 h (Figure S1-h).

As a summary of the synthetic section, we like to point out that there are several synthetic parameters such as the molar ratio of the reactants, the boiling point of the solvents, the heating rate, reaction times, *etc.*, which can be tuned to achieve the desired size of the MNPs (obviously within some limits) produced by thermal decomposition of metal (Fe, Mn, Co) precursors (Table S1). For instance, the use of solvents with higher boiling points (*e.g.*, dioctyl ether) can be used to produce bigger MNPs than the ones produced in a lower boiling point solvent (*e.g.*, benzyl ether)⁵. Longer reaction times generate in general bigger MNPs.

Table S1. Summary of the synthetic parameters used to produce different ferrite MNPs.

Sample Reactants	Mn ferrite	Co@Mn	Mn@Co-TL	Mn@Co	Co ferrite
<i>Seeds</i>	no seeds	Co ferrite (7 nm)	Mn ferrite (10 nm)	Mn ferrite (7 nm)	no seeds
<i>Precursor</i>	MnCl ₂	Mn(acac) ₂	Co(acac) ₂	Co(acac) ₂	Co(acac) ₂
<i>OLA/OLAM</i>	6.31 mmol / 12.16 mmol	2 mmol / 2 mmol	2 mmol / 2 mmol	2 mmol / 2 mmol	6 mmol / 6 mmol
<i>Solvent</i>	dioctylether (2 ml)	benzylether (20 ml)	benzylether (20 ml)	benzylether (20 ml)	benzylether (17 ml)
<i>Temperature</i>	330 °C (1 h)	300 °C (0.5 h)	300 °C (0.5 h)	300 °C(0.5 h)	300 °C (1 h)

1.3. Coating of nanoparticles using amphiphilic polymer PMA

The amphiphilic polymer was synthesized from poly (isobutylene-alt-maleic anhydride) (PMA, Mw ~6,000 g/mol, Sigma Aldrich, #531278, 39 monomers per polymer chain) and dodecylamine (DoCA, Sigma Aldrich, #D222208) following published methods⁶. The reaction product was completely dried and redissolved in anhydrous chloroform at a concentration of 0.5 M monomers (= 20 mmol / 40 ml). The polymer coating was carried out as described elsewhere⁶. The amphiphilic polymer and the “hydrophobic” core shell MNPs were mixed in a round bottom flask at a ratio $R_{p/Area}=300$, where $R_{p/Area}$ corresponds to the polymer added per nanoparticle surface unit area (nm^2). After mixing well, the solvent was slowly evaporated with a rotavap until the sample was completely dried. The residual solid film in the flask was redissolved in SBB12 buffer (sodium borate buffer, 50 mM, pH 12) under vigorous stirring until the solution turned clear. The sample was filtrated (0.22 μm , Carl Roth, # P815.1), concentrated by centrifugal filtration (Vivaspin 20, MWCO 100 kDa, Sartorius, #VS2042), and transferred into MilliQ water.

1.4. Purification of MNPs with agarose gel electrophoresis

Gel electrophoresis was used to separate polymer-coated MNPs from empty polymer micelles following published procedures⁶. The black bands in the gels, which contain the purified sample, were cut out and placed into Dialysis tubing (50 kDa molecular weight cut-off, MWCO, Sectrum Labs) with 0.5x TBE buffer. Samples were run in the electrophoresis tank (100 V, 200 mA) for 15 min, extracted from the dialysis membranes, filtered with syringe filters 0.22 μm , and concentrated with 100 kDa MWCO filters by centrifugation.

1.5. Size distribution measurements using transmission electron microscopy (TEM)

The size of the inorganic part (d_{in}) of the MNPs was determined by TEM before and after the PMA coating. Figure S1 shows TEM micrographs and size distribution of the MNPs before the PMA coating.

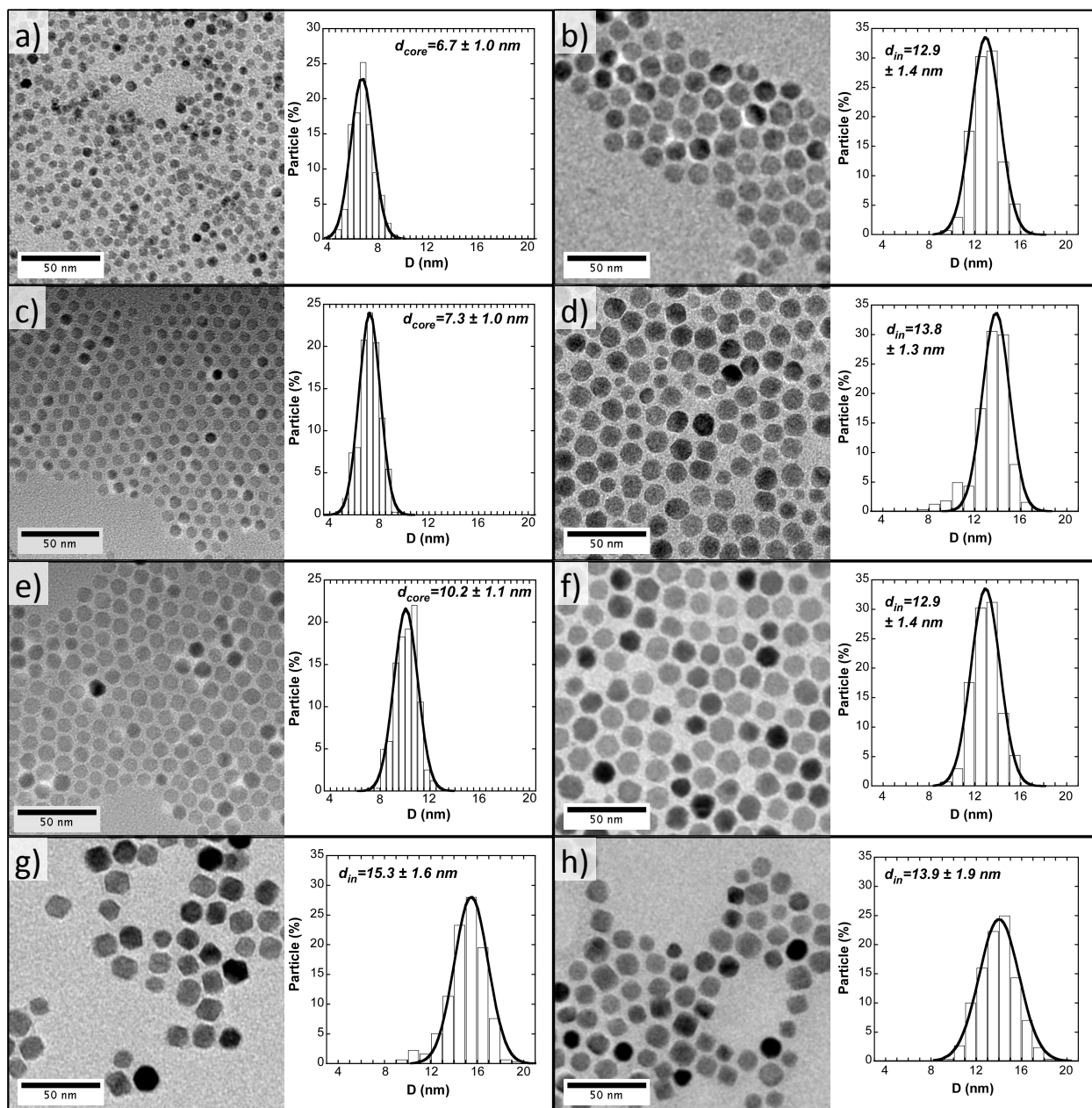


Figure S1. TEM micrographs and corresponding diameter histograms, (from > 300 MNPs, analyzed by ImageJ): **a)** Co ferrite seeds of $d_{core} = 6.7 \pm 1.0$ nm; **b)** Co@Mn NPs of $d_{in} = 12.9 \pm 1.4$ nm; **c)** Mn ferrite seeds of $d_{core} = 7.3 \pm 1.0$ nm; **d)** Mn@Co NPs of $d_{in} = 13.8 \pm 1.3$ nm; **e)** Mn ferrite seeds of $d_{core} = 10.2 \pm 1.1$ nm; **f)** Mn@Co-TL NPs of $d_{in} = 14.3 \pm 1.5$ nm; **g)** Co ferrite NPs of $d_{in} = 15.3 \pm 1.6$ nm and **h)** Mn ferrite NPs of $d_{in} = 13.9 \pm 1.9$ nm.

Further details to the negative stained TEM of the coated MNP to estimate the thickness of the PMA shell : Negatively charged carbon grids were used within 5 min after treatment to ensure hydrophilicity. The on-grid negative staining was performed using a slightly modified single-droplet negative-staining procedure. 1.5 μl sample droplet followed by three 2.5 μl droplets of 0.25% weight/volume (w/v) uranyl acetate aqueous solution were placed on a clean Parafilm piece. The treated grid was incubated on the sample droplet for 1 min and then on the staining droplets for 3 s, 3 s, and 1 min respectively. After each incubation step the excess fluid was nearly fully removed by touching the grid edge with Whatman filter paper and finally fully dried for 20 min at $2.0 \cdot 10^{-1}$ atm. Images were acquired in a JEOL JEM-1400PLUS transmission electron microscope equipped with a LaB₆ cathode running at 120kV and a GATAN US1000 CCD camera (2k x 2k) . The average thickness of the PMA shell (l_s) on the Mn@Co-TL was 2.5 – 3 nm.

1.6 Structural characterization using TEM methods

For structural transmission electron microscopic (TEM) characterization a double Cs corrected JEOL JEM-2200FS equipped with a field emission gun and working at 200kV was used. The TEM samples were prepared by applying a droplet of nanoparticles suspended in chloroform on a carbon coated TEM copper grid. After evaporation of the chloroform the nanoparticles were well distributed on the carbon film.

A high resolution scanning TEM (STEM) image of a Co-/Mn-ferrite MNP is presented in Figure S2 a). It can be seen that the particle is single crystalline without any defects. Due to the similar atomic number of Co and Mn a difference in the STEM Z-contrast of the two phases cannot be recognized. The white square marks the region from which the fast Fourier transform shown in Figure S2 b) was created.

A comparison of the experimentally obtained lattice distances with the theoretical lattice spacing of MnFe₂O₄ leads to the identification of the [12-1] zone axis. In Figure S2 c) the crystal structure for MnFe₂O₄ in [12-1] zone axis orientation simulated with VESTA [Y] is presented.

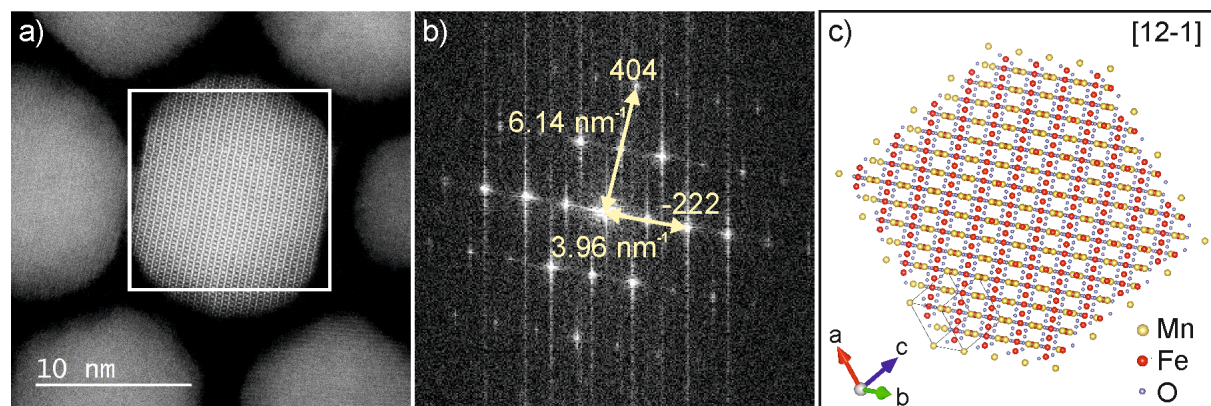


Figure S2. a) High resolution STEM image of a Co-/Mn-ferrite MNP. b) Fast Fourier transform of theregion marked by a white square in a). c) Crystal model of MnFe_2O_4 in [12-1] zone axis direction. The model was simulated with the software VESTA⁷

The composition of Mn-ferrite MNP and Mn-/Co-ferrite MNP was investigated via energy dispersive X-ray (EDX) spectroscopy in TEM mode in the same microscope using the Bruker XFlash detector 5060. Figure S3 a) shows an overlay of the spectra that have been recorded on the two different samples. Besides the signals of the MNP (Fe, Co, Mn, O) also Cu signals of the TEM grid and other signals due to the organic coating of the MNPs. An extract of Figure S3 a) is presented in Figure S3 b). The additional Co signal originating from the shell is clearly visible for the Mn-/Co-ferrite MNP.

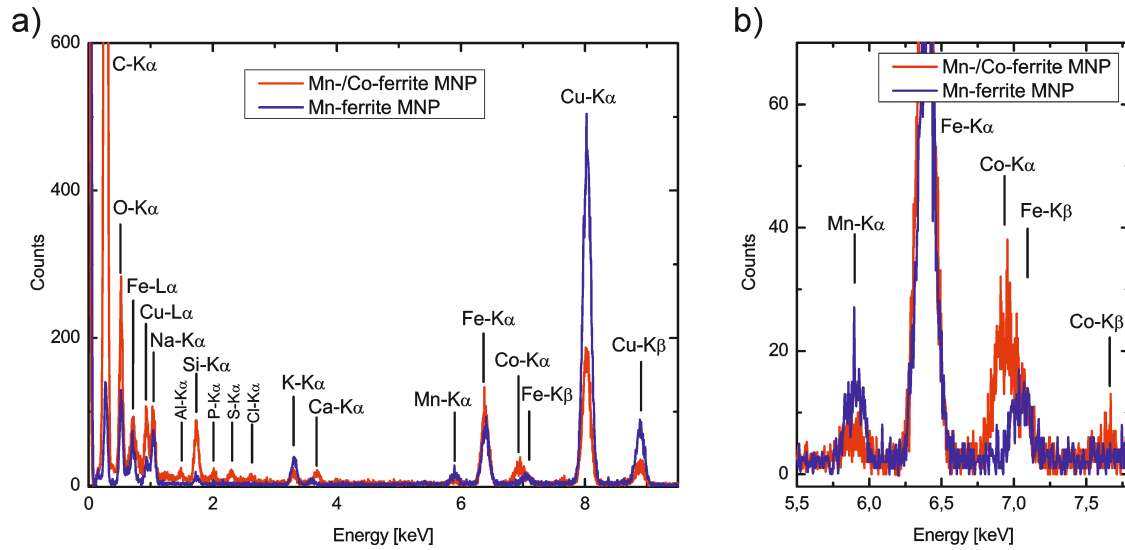


Figure S3. a) EDX spectra of Mn-ferrite MNP and Mn-/Co-ferrite MNP recorded in TEM mode. b) Extract of the spectra presented in a).

To try proving the core shell character of the MNP energy filtered transmission electron microscopy (EFTEM) was used. Electron energy loss spectra (EELS) of Co-/Mn-ferrite MNPs are presented in Figure S4. The Fe signal as well as the Mn signal of the shell are clearly resolved. However the Co signal of the core is hardly visible.

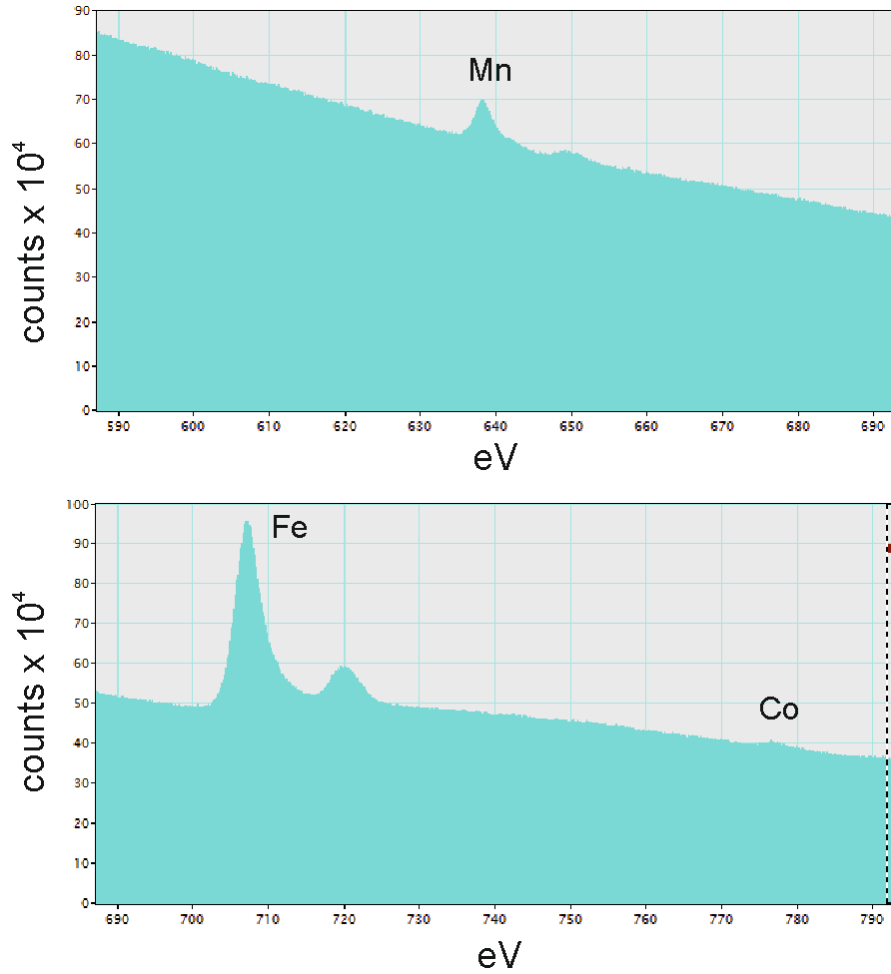


Figure S4. EELS spectra Co-/Mn-ferrite MNPs

For the EFTEM measurements the three-window-method was used. An EELS spectrum of a Mn-/Co-ferrite MNP sample and EFTEM images for C, O, Mn, Fe and Co is presented in Figure S5. In the EELS spectrum it can be seen that again the signal of the core (this time Mn) is hardly detectable. This is also represented in the EFTEM images. The elemental distribution of Co and especially Mn is extremely noisy and the data do not allow a conclusion on the structure of the MNPs. A carbon containing coverage of the MNPs is quite good resolved. Also the Fe and O distribution can be measured.

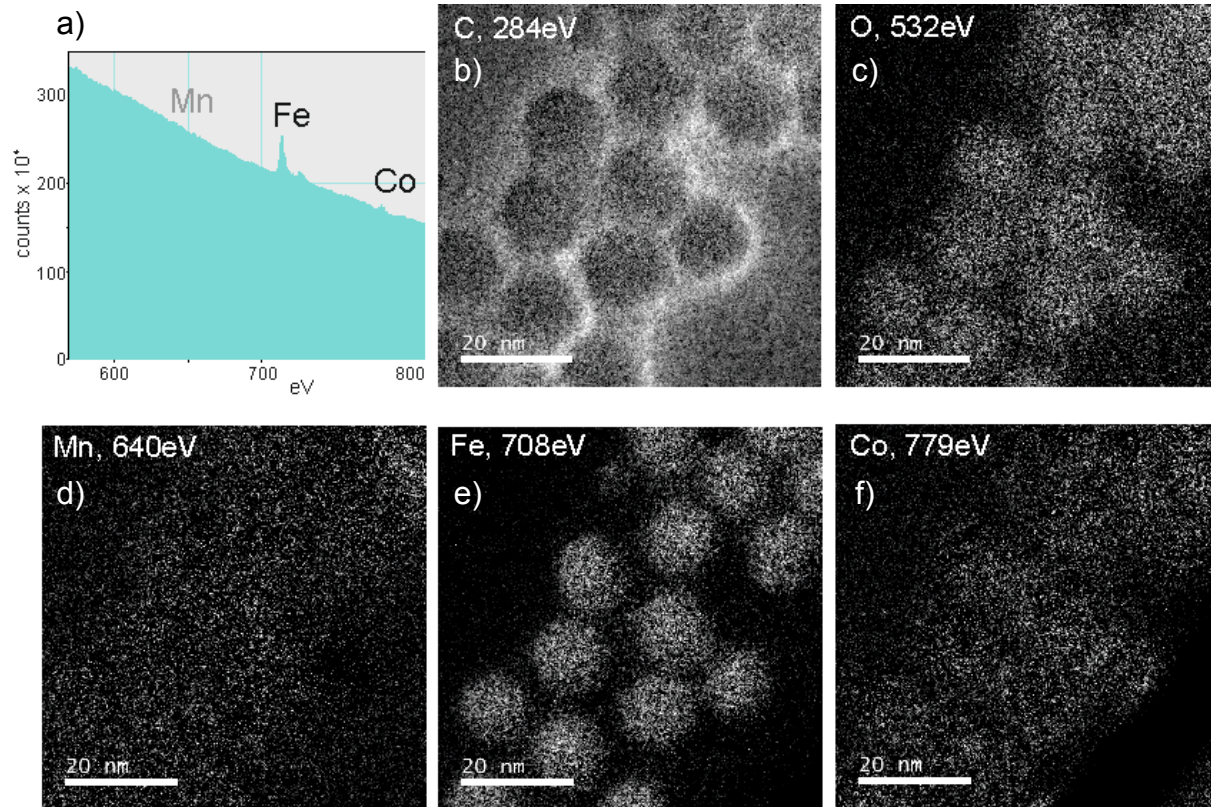


Figure S5. a) EELS spectra of Mn-/Co-ferrite MNPs. b-f) EFTEM for C, O, Mn, Fe and Co, respectively.

1.7. Dynamic light scattering (DLS) and ζ -potential

A summary of the obtained hydrodynamic diameters and ζ -potentials is shown in Table S2.

Table S2. Summary of the samples values

Sample List	N(d_h) in CHCl ₃ [nm]	N(d_h) in H ₂ O [nm]	N(ζ) [mV]
<i>Mn</i>	12.8 ± 0.02	16.8 ± 0.9	-32.4 ± 1.6
<i>Co@Mn</i>	12.5 ± 0.3	19.5 ± 0.4	-31.9 ± 1.4
<i>Mn@Co-TL</i>	12.9 ± 0.5	17.8 ± 0.9	-31.8 ± 1.3
<i>Mn@Co</i>	12.7 ± 0.5	17.1 ± 0.58	-30.7 ± 1.5
<i>Co</i>	13.1 ± 0.8	19.8 ± 2.1	-30.5 ± 0.6

1.8. ICP-MS analysis

The composition of the MNPs was analyzed by induction coupled plasma mass spectrometry (ICP-MS, Agilent 7500 Series). Following standard procedures, the contents of Fe, Co and Mn ions were obtained. For Co@Mn MNPs as example, the Fe content determined was 902 ± 33.1 ppb (parts per billion); the Co content was 28 ± 1.1 ppb and the Mn content was 139 ± 6.2 ppb. The oxygen content is not directly measured but inferred from the ratio of Fe/O in the Co/Mn-ferrite core shell structure³: $C_o = 2 \cdot C_{Fe} \cdot (M_o/M_{Fe}) = 514 \pm 18.9$ ppb. So 1 ml of Co@Mn MNP stock solution contained: $C_{Fe} = 0.9 \pm 0.03$ mg, $C_{Co} = 0.027 \pm 0.001$ mg, $C_{Mn} = 0.14 \pm 0.006$ mg, and $C_o = 2 \cdot C_{Fe} \cdot (M_o/M_{Fe}) = 0.52 \pm 0.02$ mg.

Table S3. Composition of 1 mg MNP sample as determined by ICP-MS.

Name	C _(Fe) (mg)	C _(Co) (mg)	C _(Mn) (mg)	C _(O) (mg)	Fe: Metal molar ratio
<i>Mn</i>	0.58	0	0.08	0.33	7:1
<i>Co@Mn</i>	0.56	0.02	0.09	0.32	5:1
<i>Mn@Co-TL</i>	0.55	0.11	0.03	0.31	4:1
<i>Mn@Co</i>	0.54	0.14	0.01	0.31	4:1
<i>Co</i>	0.54	0.16	0	0.31	3.5:1

2. Magnetization measurements

2.1. Instruments

Magnetic characterization has been performed directly in colloidal suspensions (M vs H measurements at RT) and in samples obtained by drying the colloidal dispersion on semi-permeable filter paper (M vs H and M vs T measurements) (instrument details see manuscript).

2.2. *Non-Interacting Super-Paramagnetic model: fit of M versus H measurements*

The magnetization M of a MNP system as a function of external field H and temperature T is

$$M = \frac{NM_0v}{V} (\coth x - 1/x) = M_s L(x) \quad x = M_0v\mu_0H/k_B T, \quad (1)$$

where N is the number of particles, v the volume of a particle, V the volume of the system, M_0 the *bulk* saturation magnetization, and $L(x)$ the Langevin function^{8,9}. The MNP's sizes in real samples are Gauss distributed around the mean hydrodynamic diameter D_h , and hence, the total magnetization of the system is not Nv , but to an integral over the measured size distribution $\int_0^{max} v \cdot f(D_h \pm \sigma) dD$:

$$M = M_s \int_0^{max} L\left(\frac{M_s v \mu_0 H}{k_B T}\right) f(D) dD \quad (2)$$

Saturation magnetization, $[M_s] = A \cdot m^2/kg$, is considered as a variable independent of the MNP or domain magnetization, $[M] = kA/m^3$, (different units are used for clarity). Both variables should be linked by the inorganic content of the sample and density. Often, domain magnetization M is fixed a priori to the theoretical value, with the fit then providing a value for the mean size and dispersity of the magnetic core. The fit of these measurements at RT provides the mean size and the standard deviation of the MNP system. The initial susceptibility $\chi_0 = M/H$ of the MNP sample can be calculated by adding the contribution of each size in the distribution of MNPs:

$$\chi_0 = \frac{\mu_0 M_s M}{3k_B T} \int_0^{\infty} V f(D) dD \quad (3)$$

It is quite usual to have small errors from the mathematical approach that is in fact unrealistic from the point of view of the physical understanding. In this particular case the non-linear minimization routine makes use of the LM (Levenberg-Marquardt) algorithm and the uncertainties are estimated by performing the square root of the diagonal elements of the covariance matrix multiplied by the MSE (Mean Square Error) or residue.

2.3. Determination of Anisotropy Constant

Fit of ZFC/FC measurements

A simple non-interacting model has been used for the fit, in which the population of MNPs (given by a size distribution $f(D)$) is sharply divided in two groups at each temperature, depending on their particular size: the fraction in an ideal superparamagnetic state that corresponds to MNPs below a certain critical volume and those, above such limit, whose super spin remains blocked:

$$M_{ZFC}(T) = \int_0^{V_c} M_s L\left(\frac{MV\mu_0 H}{k_B T}\right) f(V) dV + \int_{V_c}^{\infty} M_s \frac{M\mu_0 H}{3K_{u,c}} f(V) dV \quad (4)$$

In the first term, we make use of the low energy barrier approximation where the energy barrier (defined as $K_{eff}V$, being V the particle volume) is much smaller than the thermal energy ($k_B T$ where k_B is the Boltzmann Constant) and so can be omitted. Accordingly, the response of the magnetization to changes of magnetic field or temperature (H or T) follows a Langevin function, where M is the particle magnetization (A/m in S.I.) and M_s is the experimental saturation magnetization (including non-magnetic mass contribution, in general). Both the experimental magnetization and the particle magnetization are allowed to decrease with temperature following a spin wave-like behavior¹⁰ (Bloch type law) as:

$$M(T) = M(0)e^{-BT^{3/2}} \quad (5)$$

where the so-called Bloch constant (B) has been obtained from the magnetization measurements as a function of temperature under the maximum field of 7T, being between 2 and 4×10^{-5} in all cases.

The second term component results from the initial susceptibility of a randomly oriented magnetic domains either with uniaxial (K_u) or with cubic anisotropy (K_c), provided that $K_c > 0$, as described elsewhere¹¹. Note that K_c is the first cubic anisotropy and is equal to $4K_{eff}$ if $K_c > 0$ as in magnetite or Co ferrite. The threshold between the two populations (it is limiting both integrals) is given by a critical diameter or volume (D_C/V_C) such that:

$$V_C(T) = \frac{25k_B T}{K_{eff}(T)} \quad (6)$$

In this model, the position and shape of the ZFC maximum depends on the anisotropy through this critical volume that depends explicitly on temperature and also implicitly, through the function $K_{eff}(T)$ which is given by different models as stated in the manuscript, depending on the relative content of Co ferrite.

The expression calculated by Tachiki¹², Sloncweski¹³ and others for the anisotropy energy density of Co^{2+} takes the form of a thermal activated process as:

$$K_C = \mathcal{F}(\alpha\lambda, a, T) - \mathcal{G}(\alpha\lambda, a, T)e^{-2\mu_0\mu_B H_e/k_B T} \quad (7)$$

where ($2\mu_0\mu_B H_e$) measure the strength of the exchange field, ($\alpha\lambda$) the L-S coupling and (a) the crystal field perturbation. \mathcal{F} and \mathcal{G} are explicit functions of the L-S coupling, the crystal field splitting and the temperature

given by:

$$\mathcal{F}(\alpha\lambda, a, T) = \frac{9}{32} \frac{(\alpha\lambda)^4}{g^3} (\tanh(g/k_B T) - g/k_B T \operatorname{sech}^3(g/k_B T)) \quad (7.1)$$

and

$$\begin{aligned}
G(\alpha\lambda, a, T) = & \frac{9}{32} \frac{(\alpha\lambda)^4 \cos(g'/k_B T)}{g^3 \cos(g/k_B T)} \left[\tanh(g/k_B T) - \frac{1}{81} \frac{g^3}{g'^3} \tanh(g'/k_B T) \right. \\
& - g/k_B T \left\{ \left(1 - \frac{1}{81} \frac{g^3}{g'^3} \right) \right. \\
& \left. \left. - 2 \tanh(g/k_B T) \left(\tanh(g/k_B T) - \frac{1}{9} \frac{g}{g'} \tanh(g'/k_B T) \right) \right\} \right] \quad (7.2)
\end{aligned}$$

where

$$g = \sqrt{\frac{3}{4}(\alpha\lambda)^2 + a^2} \quad (7.3)$$

and

$$g' = \sqrt{\frac{1}{12}(\alpha\lambda)^2 + a^2} \quad (7.4)$$

2.4. *M vs H data at 5K*

Figure S6 shows hysteresis loops at 5 K of 5 samples in water dispersion and fixed (*i.e.*, deposited in a filter paper), respectively. Measurements have been normalized to 1 to easily compare the coercive fields.

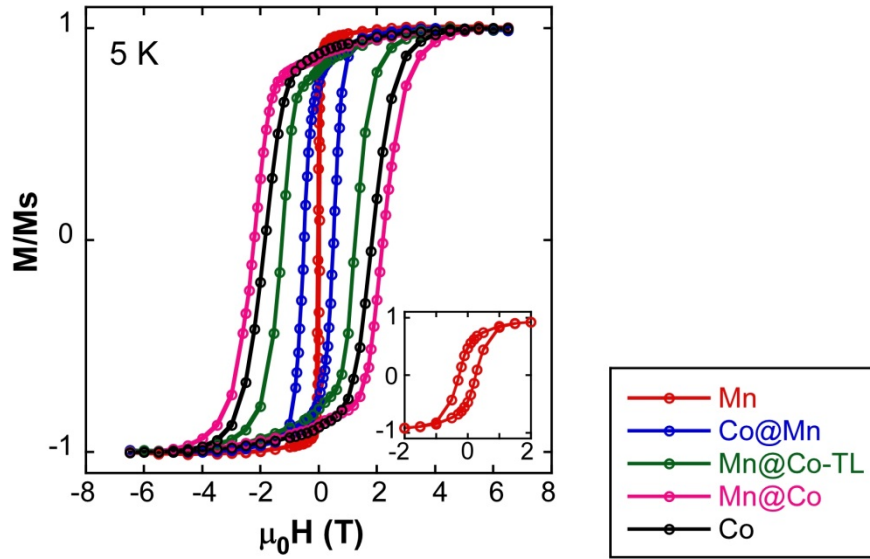


Figure S6. M vs H measurements at 5° K of the samples deposited on filter paper from aqueous dispersions (fixed NPs).

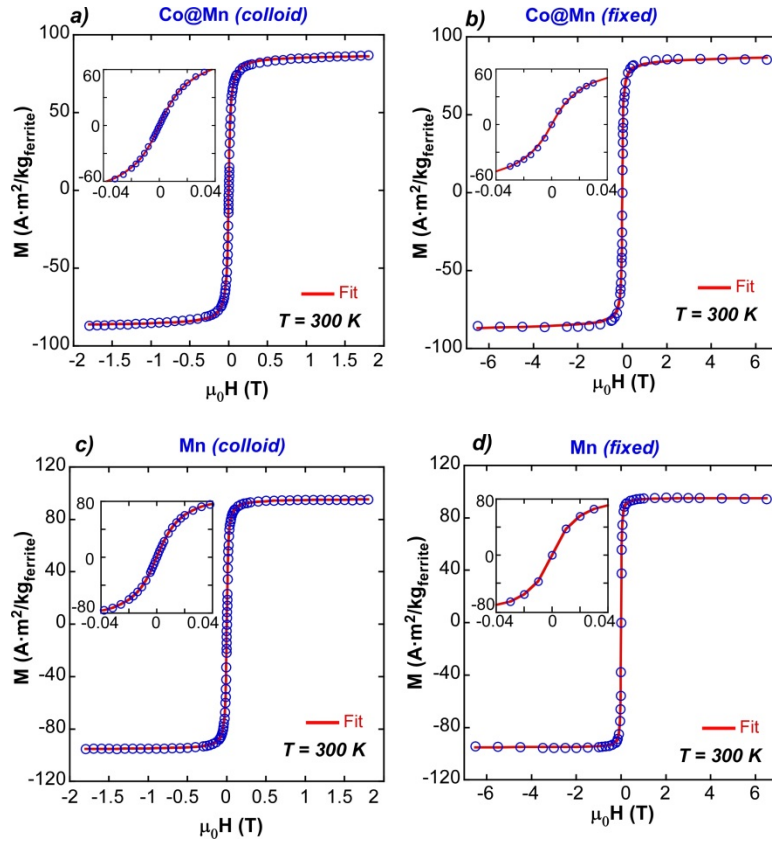
2.5. M vs H Fit and χ_0 calculation

In this case two kind of measurement at RT were carried out: **a)** directly in colloidal dispersion and **b)** in immobilized MNPs (in a filter paper). The aim of these measurements is twofold: firstly, to analyze how the initial susceptibility changes in different media and secondly, to observe empirically the effect of the removal of the Brownian contribution.

In the fits the saturation magnetization, M_s , has been fixed to the experimental value (Am^2/kg) and correspondingly the domain magnetization M (kA/m) for coherency. From Equation 3 it is obvious that the initial susceptibility is correlated with the apparent magnetic diameter d_{MvsH} .

The change of the initial susceptibility when comparing measurements in a liquid and in immobilized MNPs is thought to be a sign of the relevance of the Brownian mechanism in Co@Mn sample (Figure S3a-b). The explanation for the increase of χ_0 in liquid could be either the partial rotation of the easy axis towards the field or a significant decrease of the dipolar interactions due to the random brownian motion. Anyway, it seems that this effect happens just when the Brownian relaxation starts to be significant and so it is a direct evidence of its real weight.

In the Mn sample $K_{eff}V \ll k_B$, so it is not expected to see a change in the initial susceptibility between the sample measured in liquid and in paper. In these conditions the Neel mechanism is the only relevant relaxation process and therefore, no differences are expected in measurement in colloids and in fixed particles (Figure S7c-d).

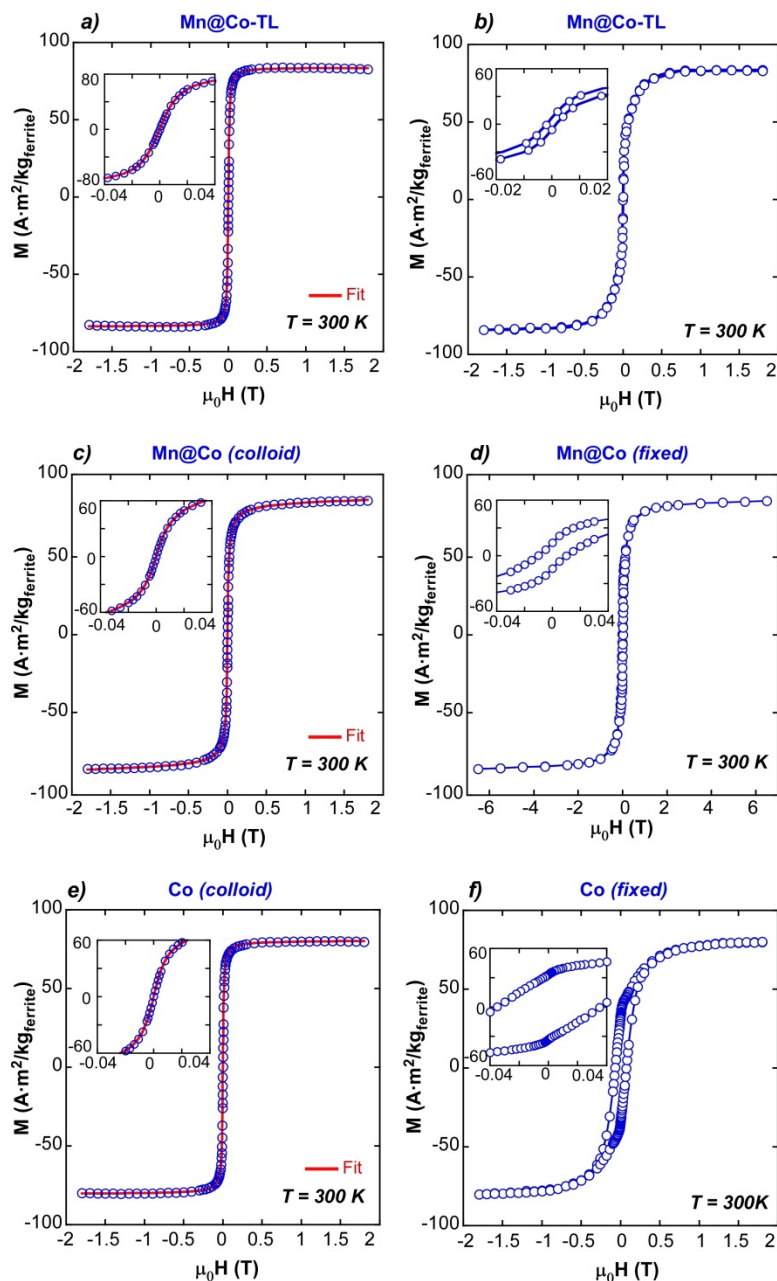


Parameter	Value (a)	Value (b)
M_s (Am^2/kg)	87 (fixed)	87 (fixed)
D (nm)	12.30 ± 0.01	10.93 ± 0.07
σ (nm)	1.50 ± 0.04	3.7 ± 0.1
χ_0 (m^3/kg)	$3.94 \cdot 10^{-3}$	$3.52 \cdot 10^{-3}$
H_c (mT)	<0.05	<0.05
M_r/M_s	<0.001	<0.001

Parameter	Value (c)	Value (d)
M_s (Am^2/kg)	90.5(fixed)	90.5(fixed)
D (nm)	13.39 ± 0.01	13.08 ± 0.05
σ (nm)	1.74 ± 0.04	2.7 ± 0.1
χ_0 (m^3/kg)	$5.44 \cdot 10^{-3}$	$5.44 \cdot 10^{-3}$
H_c (mT)	<0.05	<0.05
M_r/M_s	<0.001	<0.001

Figure S7. (a) $M(H)$ and Fit of Co@Mn in colloidal sample and (b) in fixed NPs; (c) $M(H)$ and Fit of Mn in colloidal sample and (d) in fixed NPs. The table contains the corresponding parameters of the fits at RT (D and σ) and calculated mass susceptibility.

On the other hand, in the Mn@Co-TL, Mn@Co and in Co samples (Figures S8), the MNPs do not present hysteresis above the detection limit ($50 \mu\text{T}$). In these samples when the Brownian mechanism comes into play and the MNPs show a SPM-like behavior at room temperature. On the contrary, when the MNPs are fixed in a filter paper they present hysteresis at RT, that is to say, ferromagnetic behavior. This is because at 300 K a significant percentage of MNPs are in the blocking regime.



Parameter	Value (a)	Value (b)
M_s (Am^2/kg)	84 (fixed)	84
D (nm)	14.42 ± 0.02	---
σ (nm)	1.42 ± 0.08	---
χ_0 (m^3/kg)	$5.97 \cdot 10^{-3}$	---
H_c (mT)	<0.05	1.7
M_r/M_s	<0.001	0.075

Parameter	Value (c)	Value (d)
M_s (Am^2/kg)	82 (fixed)	82
D (nm)	13.54 ± 0.02	---
σ (nm)	4.27 ± 0.03	---
χ_0 (m^3/kg)	$6.02 \cdot 10^{-3}$	---
H_c (mT)	<0.5	10.2
M_r/M_s	<0.001	0.169

Parameter	Value (e)	Value (f)
M_s (emu/g)	80 (fixed)	80
D (nm):	15.6 ± 0.02	---
σ (nm):	3.42 ± 0.05	---
χ_0 (m^3/kg):	$7.81 \cdot 10^{-3}$	---
H_c (Oe)	<0.5	70.4
M_r/M_s	<0.001	0.417

Figure S8. (a) $M(H)$ and Fit of Mn@Co-TL in colloidal sample and (b) $M(H)$ in fixed NPs; (c) $M(H)$ and Fit of Mn@Co in colloidal sample and (d) $M(H)$ in fixed NPs; (e) $M(H)$ and Fit of Co in colloidal sample and (f) $M(H)$ in fixed NPs. The table contains the corresponding parameters of the fits at RT (D and σ) and calculated mass susceptibility.

2.6. ZFC/FC measurements at different magnetic fields (1 mT and 10 mT)

Figure S9 shows ZFC/FC measurements of (a) Co@Mn, (b) Mn@Co-TL and (c) Mn@Co samples in water dispersion deposited in the filter paper at two different magnetic fields (1 and 10 mT). There is not

any significant shift in the maximum of the ZFC at different fields in the core-shell systems; so it suggests a minor influence of dipolar interaction among the MNPs.

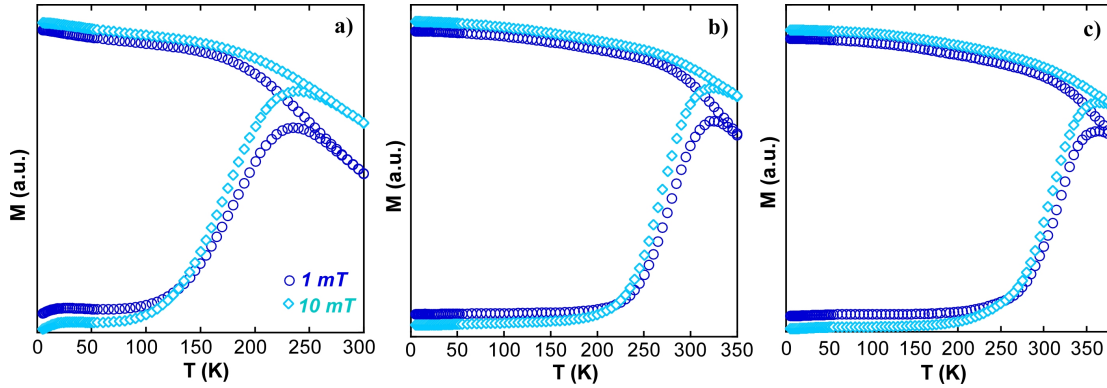


Figure S9. ZFC/FC curves at 1 mT and 10 mT fields: **(a)** Co@Mn , **(b)** Mn@Co-TL and **(c)** Mn@Co.

3. Specific Loss Power (SLP)

3.1. *Experimental equipment and measurement of SLP*




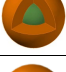
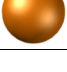
The custom built SLP measurement equipment and the measurement routine are described in the manuscript.

Temperature versus time data was recorded at 5 Hz. The dT/dt values were obtained from the slope of a linear fit to the data for the first 5 seconds of heating. SLP was calculated by using Equation 8:

$$SLP = \frac{C_{water} \cdot \rho_{water}}{\rho_{np}} \frac{dT}{dt} \quad (8)$$

where, C is the specific heat of water (4.2 J/g°C), ρ is the density of water (1 g/cm³) and ρ_{np} is the density of inorganic part of the MNPs in g/cm³. The experimental SLP data is summarized in table S4 together with the values obtained from the simulation.

Table S4 Experimental dT/dt values and SLP values of the samples.

Sample	Structure	Conc (mg/ml)	dT/dt ($^{\circ}C/s$)	SLP (W/g) Exp	SLP (W/g) Calc.
Mn		0.00256	0.112 ± 0.001	183.8 ± 1.7	190 ± 60
Co@Mn		0.00221	0.275 ± 0.005	552.6 ± 9.5	560 ± 50
Mn@Co-TL		0.00428	0.297 ± 0.001	291.4 ± 1.0	340 ± 50
Mn@Co		0.00271	0.195 ± 0.01	302 ± 15	320 ± 40
Co		0.00363	0.273 ± 0.008	315.9 ± 9.3	280 ± 30

3.2.2. Theoretical model: Basis of the simulation of SLP by Linear Response Theory (LRT) and quasi-Linear Response Theory (q-LRT)

The expected SLP for sample of MNPs with a specific mean diameter of the inorganic part d_{in} and size dispersity σ_{in} is calculated by convoluting the SLP function, $P_{SPM}(d)$, with a distribution function accounting for size distribution, $f(d_{in}, \sigma_{in})$:

$$SLP(d, \sigma) = \int_0^{d_{max}} P_{SPM}(d) f(d, \sigma) d\mathbf{d} \quad (9)$$

SLP or absorption power P_{SPM} is given in the linear approximation by¹⁴:

$$P_{SPM} = \mu_0 \pi f \chi'' H^2 \quad (10)$$

where χ'' is the imaginary part of complex susceptibility, and χ_0 the DC initial susceptibility¹⁵:

$$\chi''(\omega) = \chi_0 \frac{\omega \tau_{eff}}{1 + (\omega \tau_{eff})^2} \quad \chi_0 = \frac{\mu_0 M_S^2 V}{3k_B T} \quad (11)$$

being τ_{eff} , the effective relaxation time, resulting from the superposition of Neel relaxation (τ_N) and Brownian relaxation (τ_B), considered as independent processes¹⁶.

$$\frac{1}{\tau_{eff}} = \frac{1}{\tau_N} + \frac{1}{\tau_B} \quad (12)$$

Neel relaxation time can be calculated by¹⁷:

$$\tau_N = \frac{\tau_0}{2} \left(\frac{\pi k_B T}{KV} \right)^{1/2} e^{KV/k_B T} \quad (13)$$

where τ_0 is the inverse of the so-called frequency of jump attempts, usually between 10^{-9} and 10^{-11} s. V is the MNP volume, K the effective anisotropy constant and k_B is the Boltzmann constant.

The Brownian relaxation time is given by:

$$\tau_B = \frac{4\pi\eta r_h^3}{k_B T} \quad (14)$$

Where η is the viscosity of the solvent, and r_h the hydrodynamic radius.

It is important to underline that the previous model can be corrected for a quasi-Linear Response by using a modified susceptibility, the so-called chord susceptibility¹⁸ given by:

$$\chi_{\text{chord}} = \frac{M_S L(\xi)}{H_{\text{max}}} \quad (15)$$

Note that in this framework, the non-linearity is included in this susceptibility that becomes dependent on the amplitude of the AC excitation.

References:

- (1) Sun, S.; Zeng, H.; Robinson, D. B.; Raoux, S.; Rice, P. M.; Wang, S. X.; Li, G. Monodisperse MFe₂O₄ (M = Fe, Co, Mn) Nanoparticles. *J. Am. Chem. Soc.* **2004**, *126*, 126–132.
- (2) Chen, R.; Christiansen, M. G.; Anikeeva, P. Maximizing Hysteretic Losses in Magnetic Ferrite Nanoparticles via Model-Driven Synthesis and Materials Optimization. *ACS Nano* **2013**, *7*, 8990–9000.
- (3) Lee, J.-H.; Jang, J.-T.; Choi, J.-S.; Moon, S. H.; Noh, S.-H.; Kim, J.-W.; Kim, J.-G.; Kim, I.-S.; Park, K. I.; Cheon, J. Exchange-Coupled Magnetic Nanoparticles for Efficient Heat Induction. *Nat. Nanotechnol.* **2011**, *6*, 418–422.
- (4) Sun, S.; Zeng, H. Size-Controlled Synthesis of Magnetite Nanoparticles. *J. Am. Chem. Soc.* **2002**, No. 31, 8204–8205.

- (5) Xie, J.; Peng, S.; Brower, N.; Pourmand, N.; Wang, S. X.; Sun, S. One-Pot Synthesis of Monodisperse Iron Oxide Nanoparticles for Potential Biomedical Applications. *Pure Appl. Chem.* **2006**, *78*, 1003–1014.
- (6) Lin, C.-A. J.; Sperling, R. A.; Li, J. K.; Yang, T.-Y.; Li, P.-Y.; Zanella, M.; Chang, W. H.; Parak, W. J. Design of an Amphiphilic Polymer for Nanoparticle Coating and Functionalization. *Small* **2008**, *4*, 334–341.
- (7) Momma, K.; Izumi, F. *VESTA 3* for Three-Dimensional Visualization of Crystal, Volumetric and Morphology Data. *J. Appl. Crystallogr.* **2011**, *44*, 1272–1276.
- (8) Kaiser, R. Magnetic Properties of Stable Dispersions of Subdomain Magnetite Particles. *J. Appl. Phys.* **1970**, *41*, 1064.
- (9) Weaver, J. B.; Rauwerdink, A. M.; Hansen, E. W. Magnetic Nanoparticle Temperature Estimation. *Med. Phys.* **2009**, *36*, 1822–1829.
- (10) Aquino, R.; Depeyrot, J.; Sousa, M. H.; Tourinho, F. a.; Dubois, E.; Perzynski, R. Magnetization Temperature Dependence and Freezing of Surface Spins in Magnetic Fluids Based on Ferrite Nanoparticles. *Phys. Rev. B* **2005**, *72*, 184435.
- (11) Chikazumi, S. *Physics of Ferromagnetism*; Oxford University Press, 2009.
- (12) Tachiki, M. Origin of the Magnetic Anisotropy Energy of Cobalt Ferrite. *Prog. Theor. Phys.* **1960**, *23*, 1055–1072.
- (13) Slonczewski, J. C. Origin of Magnetic Anisotropy in Cobalt-Substituted Magnetite. *Phys. Rev.* **1958**, *110*, 1341–1348.
- (14) Kita, E.; Oda, T.; Kayano, T.; Sato, S.; Minagawa, M.; Yanagihara, H.; Kishimoto, M.; Mitsumata, C.; Hashimoto, S.; Yamada, K.; et al. Ferromagnetic Nanoparticles for Magnetic Hyperthermia and Thermoablation Therapy. *J. Phys. D. Appl. Phys.* **2010**, *43*, 474011.
- (15) Coral, D. F.; Mendoza Zélis, P.; de Sousa, M. E.; Muraca, D.; Lassalle, V.; Nicolás, P.; Ferreira, M. L.; Fernández van Raap, M. B. Quasi-Static Magnetic Measurements to Predict Specific Absorption Rates in Magnetic Fluid Hyperthermia Experiments. *J. Appl. Phys.* **2014**, *115*, 043907.
- (16) Hergt, R.; Dutz, S.; Müller, R.; Zeisberger, M. Magnetic Particle Hyperthermia: Nanoparticle Magnetism and Materials Development for Cancer Therapy. *J. Phys. Condens. Matter* **2006**, *18*, S2919–S2934.
- (17) Brown, W. F. Thermal Fluctuations of a Single-Domain Particle. *Phys. Rev.* **1963**, *130*, 1677–1686.
- (18) Rosensweig, R. E. Heating Magnetic Fluid with Alternating Magnetic Field. *J. Magn. Magn. Mater.* **2002**, *252*, 370–374.